Front. Chem. Sci. Eng. 2023, 17(4): 437–448
https://doi.org/10.1007/s11705-022-2228-1

RESEARCH ARTICLE

Oxygen-deficient MoO_x/Ni_3S_2 heterostructure grown on nickel foam as efficient and durable self-supported electrocatalysts for hydrogen evolution reaction

Zihuan Yu[1], Haiqing Yan[1], Chaonan Wang[1], Zheng Wang[1], Huiqin Yao (✉)[2], Rong Liu (✉)[3], Cheng Li (✉)[4], Shulan Ma (✉)[1]

1 Beijing Key Laboratory of Energy Conversion and Storage Materials, College of Chemistry, Beijing Normal University, Beijing 100875, China
2 School of Basic Medical Sciences, Ningxia Medical University, Yinchuan 750004, China
3 Analytical and Testing Center, Beijing Normal University, Beijing 100875, China
4 Shanghai Institute of Applied Physics, Chinese Academy of Sciences, Shanghai 201800, China

Abstract High-performance and ultra-durable electrocatalysts are vital for hydrogen evolution reaction (HER) during water splitting. Herein, by one-pot solvothermal method, MoO_x/Ni_3S_2 spheres comprising Ni_3S_2 nanoparticles inside and oxygen-deficient amorphous MoO_x outside *in situ* grow on Ni foam (NF), to assembly the heterostructure composites of MoO_x/Ni_3S_2/NF. By adjusting volume ratio of the solvents of ethanol to water, the optimized MoO_x/Ni_3S_2/NF-11 exhibits the best HER performance, requiring an extremely low overpotential of 76 mV to achieve the current density of 10 $mA{\cdot}cm^{-2}$ (η_{10} = 76 mV) and an ultra-small Tafel slope of 46 $mV{\cdot}dec^{-1}$ in 0.5 $mol{\cdot}L^{-1}$ H_2SO_4. More importantly, the catalyst shows prominent high catalytic stability for HER (> 100 h). The acid-resistant MoO_x wraps the inside Ni_3S_2/NF to ensure the high stability of the catalyst under acidic conditions. Density functional theory calculations confirm that the existing oxygen vacancy and MoO_x/Ni_3S_2 heterostructure are both beneficial to the reduced Gibbs free energy of hydrogen adsorption ($|\Delta G_{H^*}|$) over Mo sites, which act as main active sites. The heterostructure effectively decreases the formation energy of O vacancy, leading to surface reconstruction of the catalyst, further improving HER performance. The MoO_x/Ni_3S_2/NF is promising to serve as a highly effective and durable electrocatalyst toward HER.

Keywords molybdenum oxides, oxygen vacancies, heterostructure, electrocatalysts, hydrogen evolution reaction

Received May 6, 2022; accepted July 27, 2022

E-mails: huiqin_yao@163.com (Yao H.), liur@bnu.edu.cn (Liu R.), licheng@sinap.ac.cn (Li C.), mashulan@bnu.edu.cn (Ma S.)

1 Introduction

With the fast growth of energy demands and deterioration of environment, it is necessary to develop renewable and clean energy [1]. Hydrogen (H_2), thanks to its environmental friendliness and high energy density, has attracted great attention [2]. Electrocatalytic water splitting has be considered as the most eco-friendly and economical route to produce H_2, because water is an abundant and renewable source [3]. However, the hydrogen evolution reaction (HER) during water electrolysis suffers from large overpotential and slow kinetics [4]. To speed up the HER kinetics, highly active and durable electrocatalysts are applied to lower the dynamic overpotentials [5]. Pt-based compounds have been considered as the most efficient electrocatalysts toward HER, but the preciousness and scarcity of Pt seriously restrict its practical utilization in water electrolysis [6]. Thus, it is vital to explore low-cost while high-efficiency electrocatalysts to replace Pt-based materials.

Nonprecious metal materials, such as Mo-based sulfides [7], oxides [8], phosphides [9], and carbides [10], have been investigated as potential HER catalysts. Compared with molybdenum sulfides, molybdenum oxides are highly stable and readily available in large scale and can also show acceptable HER property [11]. MoO_3 (α-MoO_3), as a low-price and nontoxic material, has been reported to be widely applied in HER, exhibiting an overpotential of 112 mV achieving the current density of 10 $mA{\cdot}cm^{-2}$ (η_{10} = 112 mV) in acid media [12]. However, because of the less active sites and poor conductivity of intrinsic MoO_3, its catalytic performance

has been reported to be much lower than that of Pt-based materials [13]. If the MoO_3 is combined with other substances to fabricate certain active interfaces, the active sites of MoO_3 may be exposed as much as possible [14]. Zhang's group [15] coupled MoO_3 with 1T'-MoS_2 to assembly 1T'-MoS_2/MoO_3 heterostructure nanosheets, in which the MoS_2/MoO_3 interfaces can facilitate electron transfer and surface hydrogen generation, leading to the improvement of electrocatalytic performance. Besides, loading P element onto MoO_3 nanosheets can also improve the HER catalytic performance [16], for which the P component can boost the adsorption/desorption of proton and afterwards increase electrocatalytic performance. A composite electrocatalyst comprising RuO_2 supported on MoO_3 nanosheets was investigated as an HER electrocatalyst, in which the synergetic effect created through interaction between MoO_3 and RuO_2 led to the enhancement of catalytic activity [17]. Nevertheless, their HER performance is still inferior to that of precious metals. In addition, the oxygen vacancy in MoO_3 may not only produce greater conductivity, but also act as HER active site [13]. For example, MoO_{3-x} with oxygen vacancies depicted higher HER catalytic activity than com-MoO_3 [13]. Density functional theory (DFT) calculation revealed that the oxygen vacancy prominently reduces the adsorption energy of H_2O and then improves the catalytic activity. Thus, fabricating oxygen vacancies and active interfaces into molybdenum oxides may be effective ways to enhance the HER performance of molybdenum oxides. The known researches on molybdenum oxides with oxygen vacancy are all about crystalline MoO_3, but there are lack of reports focused on amorphous MoO_x with oxygen vacancy.

Meanwhile, Ni-based materials have shown a big potential for using as HER catalysts [18]. Ni_3S_2, because of the existence of Ni–Ni networks throughout its crystal structure, exhibits good metallic conductivity [19]. So far, many studies revealed that Ni_3S_2 owns HER activity [20], while its catalytic activity and stability are still less competitive relative to noble-metal catalysts. On the other hand, self-supported catalysts, compared to powdery ones, avoid the addition of polymer binder. Meanwhile, the introduction of substrates in self-supporting catalysts can raise electrochemical active areas. The three-dimensional nickel foam (NF) is a low-cost template with large surface area, and is normally used as a conductive substrate to host electrocatalyst materials [21]. Using thiourea, $Ni(NO_3)_2{\cdot}6H_2O$ and NF as reactants, Ni_3S_2/NF was fabricated to depict high HER activity and good durability in basic and neutral conditions [22]. Hybridizing Ni_3S_2 with other electrocatalysts such as MoS_2 [23] and/or Co_9S_8/MoS_2 [24] is also a commonly employed method to augment the catalytic activity. Moreover, Ni_3S_2 is generally combined with other sulfides, while the integration of Ni_3S_2 with amorphous MoO_x is rarely reported. As known, Ni_3S_2 and NF matrix are unstable in acidic solutions, while MoO_3 or MoO_x is acid-resistant. Therefore, if NF and the *in situ* grown Ni_3S_2 are wrapped by dense layers of MoO_x, it is expected to improve the acid resistance of the integrated elelctrocatalysts.

Herein, via a facile solvothermal method, we fabricate MoO_x/Ni_3S_2 spheres which consist of dispersed Ni_3S_2 nanoparticles and amorphous MoO_x wrapped outside. By adjusting ratios of water/ethanol solvents, the as-prepared MoO_x/Ni_3S_2/NF-11 (volume ratio of ethanol:water is 1:1) exhibits optimum HER performance, requiring an extremely low overpotential (η_{10} = 76 mV) and a much low Tafel slope of 46 mV·dec^{-1} in 0.5 mol·L^{-1} H_2SO_4. Benefiting from the existing oxygen vacancy and formed heterojunction, Mo atoms are exposed as much as possible to exhibit reduced Gibbs free energy of hydrogen adsorption (ΔG_{H^*}) and act as active-sites. Additionally, the stability of the catalyst under acidic conditions is greatly improved because the acid-resistant amorphous MoO_x layer is wrapped around Ni_3S_2/NF. The MoO_x/Ni_3S_2/NF-11 displays extremely high stability (⩾ 100 h at 23.5 mA·cm^{-2}). This study would give a novel perspective on the fabrication of amorphous molybdenum oxides or oxygen-deficient materials with excellent HER performance.

2 Experimental

2.1 Synthesis of MoO_x/Ni_3S_2/NF composites

A series of MoO_x/Ni_3S_2/NF composites (labeled as MoO_x/Ni_3S_2/NF-*mn*, where *m* and *n* are volume ratios of ethanol:water) were synthesized via a one-pot solvothermal reaction. Typically, two pieces of commercial NF (1 cm × 2 cm) were first immersed in an acid solution (1 mol·L^{-1} HCl) for 20 min, to remove the oxides on the surface of NF. Then the NF was washed using acetone, water and ethanol in turn, and then was dried in vacuum at 45 °C, followed by weighing. Meanwhile, 2 mmol of $Na_2MoO_4{\cdot}2H_2O$ was dissolved in 30 mL of ethanol:water mixture solvents. After stirred for 30 min, 10 mmol of thiourea was dissolved in the solutions. The abovementioned solutions and pre-treated NF were simultaneously transferred to a Teflon-lined autoclave (50 mL) and reacted at 140 °C for 18 h. After cooled, the obtained MoO_x/Ni_3S_2/NF-*mn* products were washed with excess deionized water and ethanol several times, and then dried in vacuum at 45 °C overnight.

2.2 Electrochemical measurements

The electrochemical tests were conducted in a three-electrode cell in a 0.5 mol·L^{-1} H_2SO_4 solution. Ag/AgCl (saturated KCl) electrode and a graphite rod electrode worked as reference and counter electrodes, respectively.

The as-prepared samples were used directly as working electrodes. For a reliable comparison, we loaded Pt–C and commercial MoO_3 (com-MoO_3) on NF with the same mass loading as MoO_x/Ni_3S_2/NF-11. Table S1 (cf. Electronic Supplementary Material, ESM) listed the mass loading of all catalysts. The details of electrochemical measurements are shown in ESM.

3 Results and discussion

3.1 Material characterization

The fabrication procedure of the MoO_x/Ni_3S_2/NF composites is described in Scheme 1. In the solvothermal reaction, the thiourea may break down to release HS^- ions (Eq. (1)); meantime, the NF can release Ni^{2+} into the solution, and the Ni^{2+} would react with the active HS^- to generate the Ni_3S_2 particles (Eq. (2)) [24]:

$$NH_2CSNH_2 + 3H_2O \rightarrow 2NH_4^+ + HS^- + HCO_3^- \quad (1)$$

$$3Ni + 2HS^- + 2H_2O \rightarrow Ni_3S_2 + 2OH^- + 2H_2 \quad (2)$$

The structures of the MoO_x/Ni_3S_2/NF-*mn* were studied firstly by X-ray diffraction (XRD) measurements. As shown in Fig. 1, for all samples, there appeared diffraction peaks at 21.7°, 31.1°, 37.8°, 49.7° and 55.2° respectively assigned to the (101), (110), (003), (113) and (122) planes of hexagonal Ni_3S_2 (JCPDS no. 44-1418) [25]. This indicates that the partial NF surface was converted to Ni_3S_2 under the solvothermal conditions. Three strong diffraction peaks of Ni were derived from the NF substrate. However, no distinguishable diffractions related to MoO_x were found, suggesting that if there is certain MoO_x phase, it would exist in amorphous form. The transmission electron microscope (TEM) characterization discussed below with the absence of lattice fringes would provide important evidence of the amorphous characteristic.

The morphologies of NF (Fig. S1, cf. ESM) and MoO_x/Ni_3S_2/NF-*mn* (Fig. 2) were characterized by scanning electron microscopy (SEM). Figure S1(a) shows the 3D porous characteristic of NF, and at higher magnification, the surface of NF can be observed to be very smooth (Fig. S1(a′)). The special skeleton of NF provides large surface area and ideal mechanical stability. As seen in Fig. 2, the entire NF surface is tightly covered by the MoO_x/Ni_3S_2. When ethanol solvent was absent in the reaction (no ethanol), the resulting product of MoO_x/Ni_3S_2/NF-01 (Figs. 2(a) and 2(a′)) has some cracks on its surface, which may reduce the conductivity of the catalyst [26]. At the ethanol:water ratio of 1:1, the as-formed MoO_x/Ni_3S_2/NF-11 presents irregular small spheres grown on the substrate (Figs. 2(b) and 2(b′)). In addition, it can be seen from Fig. 2(b) that there is no

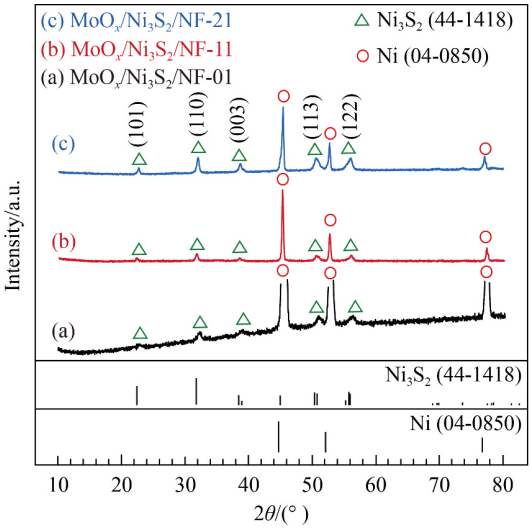

Fig. 1 XRD patterns of (a) MoO_x/Ni_3S_2/NF-01, (b) MoO_x/Ni_3S_2/NF-11 and (c) MoO_x/Ni_3S_2/NF-21.

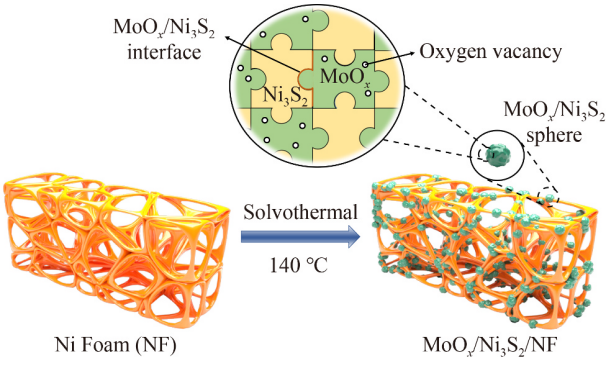

Scheme 1 Schematic illustration of formation of oxygen-deficient MoO_x/Ni_3S_2/NF composites.

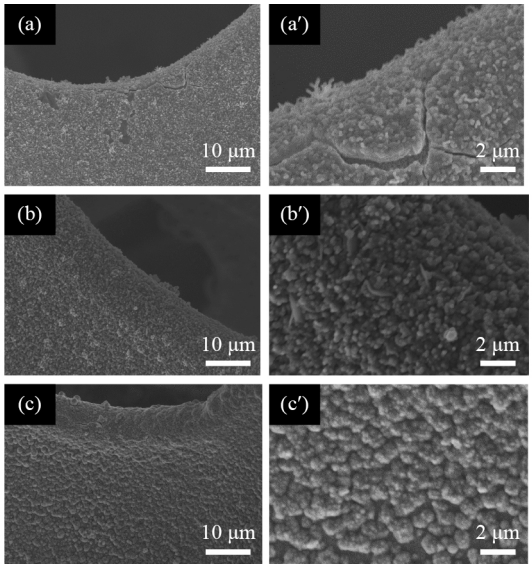

Fig. 2 SEM images of (a, a′) MoO_x/Ni_3S_2/NF-01, (b, b′) MoO_x/Ni_3S_2/NF-11 and (c, c′) MoO_x/Ni_3S_2/NF-21.

crack on the surface of the sample, which means that the acid-resistant NF matrix is completely coated by MoO_x/Ni_3S_2, so that NF cannot be corroded by acid, paving the way for the excellent stability of the catalyst under acidic conditions. As the ethanol:water ratio is increased to 2:1 (with more ethanol), as found in MoO_x/Ni_3S_2/NF-21, the formed MoO_x/Ni_3S_2 spheres on the NF surface become larger (Figs. 2(c) and 2(c′)).

For the MoO_x/Ni_3S_2/NF-11 with the most regular and perfect appearance, detailed morphology and structure were further explored by TEM (Figs. 3 and S3, cf. ESM) via scratching the samples from the NF substrate. TEM images (Figs. 3(a) and 3(b)) show that the MoO_x/Ni_3S_2 spheres are comprised of nanoparticles. Figure 3(c) reveals the interface region of the Ni_3S_2 nanoparticles, indicating that there are two clearly distinguishable phases between the inside and outside of the particle, and the Ni_3S_2 nanoparticle is closely connected to the amorphous MoO_x. For clarity, the original image (without scaling) of Fig 3(c) is shown in Fig. S2 (cf. ESM). The TEM investigations of MoO_x/Ni_3S_2-11 (see Figs. 3(d) and 3(e)) further exhibit the tight connection between the Ni_3S_2 particles and MoO_x. The lattices of 0.24 (Fig. 3(d)) and 0.29 nm (Fig. 3(e)) are ascribed to (003) and (110) crystal planes of Ni_3S_2 [27], further proving its presence. The above results can be supported by the SAED pattern (Fig. 3(f)), which displays characteristic crystal planes of Ni_3S_2 and diffuse rings of the amorphous MoO_x. The amorphous characteristic of MoO_x leads to the absence of XRD diffractions (see Fig. 1). The MoO_x surrounding for Ni_3S_2 further ensures the acid resistance of the electrocatalyst. The compositional distributions of the MoO_x/Ni_3S_2-11 sphere are confirmed by elemental mapping analyses (Fig. 3(g)), high angle annular dark field scanning transmission electron microscope (HAADF-STEM) image (Fig. S3(a)) and line scans (Fig. S3(b)). In Fig. 3(g), uneven distribution of Mo/O and Ni/S is clearly observed throughout the whole sphere. The elements of Mo and O appear in the same region, while Ni and S elements locate in other regions, indicating that the two

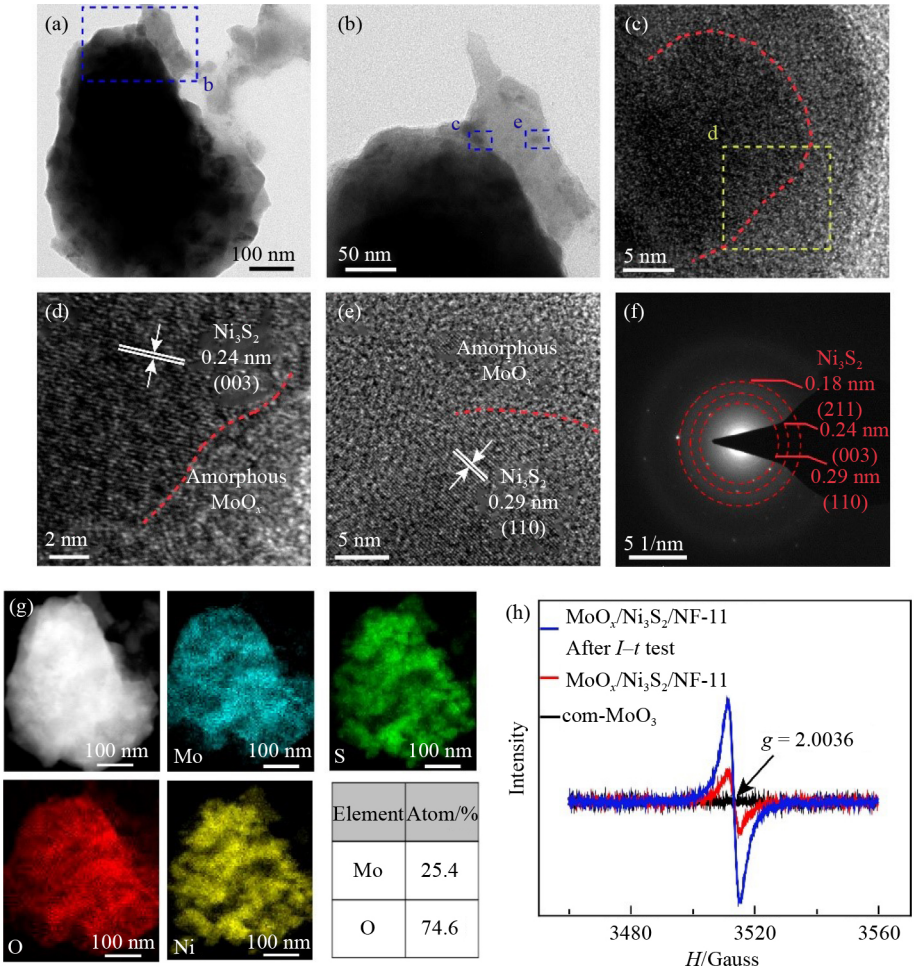

Fig. 3 (a, b) TEM images of MoO_x/Ni_3S_2-11, (c, d, e) HR-TEM images of MoO_x/Ni_3S_2-11, and the visible lattice fringes images obtained from the blue and yellow square regions; (f) SAED pattern of MoO_x/Ni_3S_2-11; (g) HAADF-STEM and energy dispersive spectroscopy elemental mappings of Mo, O and Ni of MoO_x/Ni_3S_2-11; (h) electron paramagnetic resonance (EPR) spectrum of MoO_x/Ni_3S_2/NF-11 before and after 60 h *I*–*t* test, and the control sample of com-MoO_3.

phases of MoO_x and Ni_2S_3 have distinct interfaces. From Fig. 3(g), the atom ratio of Mo:O is 1:2.94, which is close to MoO_3, with the oxygen content slightly reduced. All these results prove the existence of Ni_3S_2 crystalline phase along with amorphous MoO_x.

To clarify the detailed structure of MoO_x/Ni_3S_2/NF-11, EPR spectroscopy and X-ray photoelectron spectroscopy (XPS) were carried out and the results were shown in Fig. 4, with com-MoO_3 as a control sample. In Fig. 3(h), the EPR spectra of com-MoO_3 (black line) shows no signal, while MoO_x/Ni_3S_2/NF-11 (red line) displays a signal at about 3512 Guass (g = 2.0036), indicating the existence of oxygen vacancy. For XPS spectra of MoO_x/Ni_3S_2/NF-11 (Fig. 4(a)), the binding energies of 235.6 and 232.4 eV are related to Mo $3d_{3/2}$ and $3d_{5/2}$ of Mo^{6+}, the same as found in com-MoO_3 [28]. In contrast to com-MoO_3, MoO_x/Ni_3S_2/NF-11 shows a pair of peaks of Mo^{5+} (234.0 eV for Mo $3d_{3/2}$ and 230.8 eV for Mo $3d_{5/2}$) [29]. Comparison of O 1s spectra of MoO_x/Ni_3S_2/NF-11 and com-MoO_3 is presented in Fig. 4(b). As shown, for com-MoO_3, the binding energy of 531.9 eV is assigned to lattice oxygen (O^{2-}) [30], while in MoO_x/Ni_3S_2/NF-11, the energy of O^{2-} is reduced to a lower level (531.5 eV). Also, the half-peak width of O 1s core-level spectra of the MoO_x/Ni_3S_2/NF-11 is widened in comparison with that of the com-MoO_3. The difference of half-peak width of O 1s core-level spectra in the materials with and without oxygen vacancies has also been observed in other literature [31]. For MoO_x/Ni_3S_2/NF-11, the appearance of Mo^{5+} and the shift of O 1s simultaneously prove the presence of oxygen vacancy, which is consistent with EPR results. All these indicate a changed coordination configuration between Mo and O, as discussed in literatures [13,16]. It was reported that the shift of O 1s to a lower energy level means the electron transfer to the neighboring oxygen vacancies [32]. Meanwhile, one weak peak detected at 533.4 eV can be assigned to O 1s of surface adsorbed species (here is OH^-) [33]. In Fig. 4(c), for Ni 2p spectra of MoO_x/Ni_3S_2/NF-11, the peaks at 873.8 and 856.0 eV are related to Ni $2p_{1/2}$ and Ni $2p_{3/2}$ of Ni^{2+}, accompanied by two satellite peaks at 879.8 and 861.7 eV [34]. The peak at 853.4 eV is assigned to Ni^0, which belongs to Ni_3S_2 or NF [35]. In the spectra of S 2p (Fig. 4(d)), the two signals at 162.9 and 161.7 eV belong to $2p_{1/2}$ and $2p_{3/2}$ of S^{2-}, and the other two signals at 164.4 and 163.2 eV are attributed to $2p_{1/2}$ and $2p_{3/2}$ of S_2^{2-} [36], suggesting the presence of terminal unsaturated S of Ni–S bonds [37]. The peak at 168.2 eV is assigned to oxidized sulfur species (here is SO_4^{2-}) owing to surface oxidation [38]. In Raman spectra of MoO_x/Ni_3S_2/NF-11 (Fig. S4, cf. ESM), the band at 324 cm^{-1} is associated with A_1 vibration mode of the Ni_3S_2 phase [39], and the

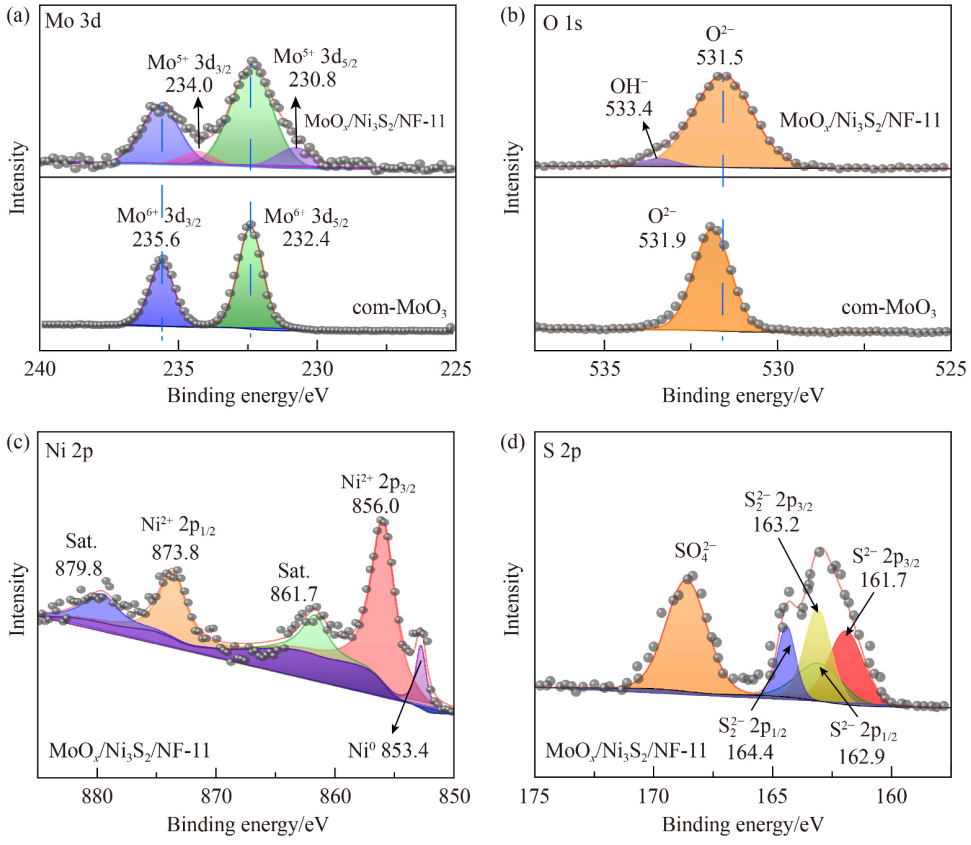

Fig. 4 X-ray photoelectron spectra with deconvolution of (a) Mo 3d, (b) O 1s for MoO_x/Ni_3S_2/NF-11 and com-MoO_3, (c) Ni 2p, and (d) S 2p for MoO_x/Ni_3S_2/NF-11.

peaks ranging from 800 to 1000 cm^{-1} are related to Mo=O modes [16]. We also measured the infrared spectrum of MoO_x/Ni_3S_2/NF-11 (Fig. S5, cf. ESM). The bands at 975 and 914 cm^{-1} correspond to the stretching vibration of Mo=O, and the bands at 615 and 514 cm^{-1} are assigned to stretching and bending vibrations of Mo–O, respectively [40]. No Mo–S related spectral peaks can be observed, which proves that the sample does not contain Mo–S bond.

3.2 Electrocatalytic performance for HER

HER performance of MoO_x/Ni_3S_2/NF-*mn* synthesized at different ethanol:H_2O ratios and control samples of com-MoO_3/NF, Ni_3S_2/NF and Pt–C/NF was measured (Fig. 5 and Fig. S6, cf. ESM). As observed (Fig. S6), among the three samples, the MoO_x/Ni_3S_2/NF-11 at an ethanol:H_2O ratio of 1:1 exhibits an extremely low η_{10} value of 76 mV, demonstrating HER performance much better than

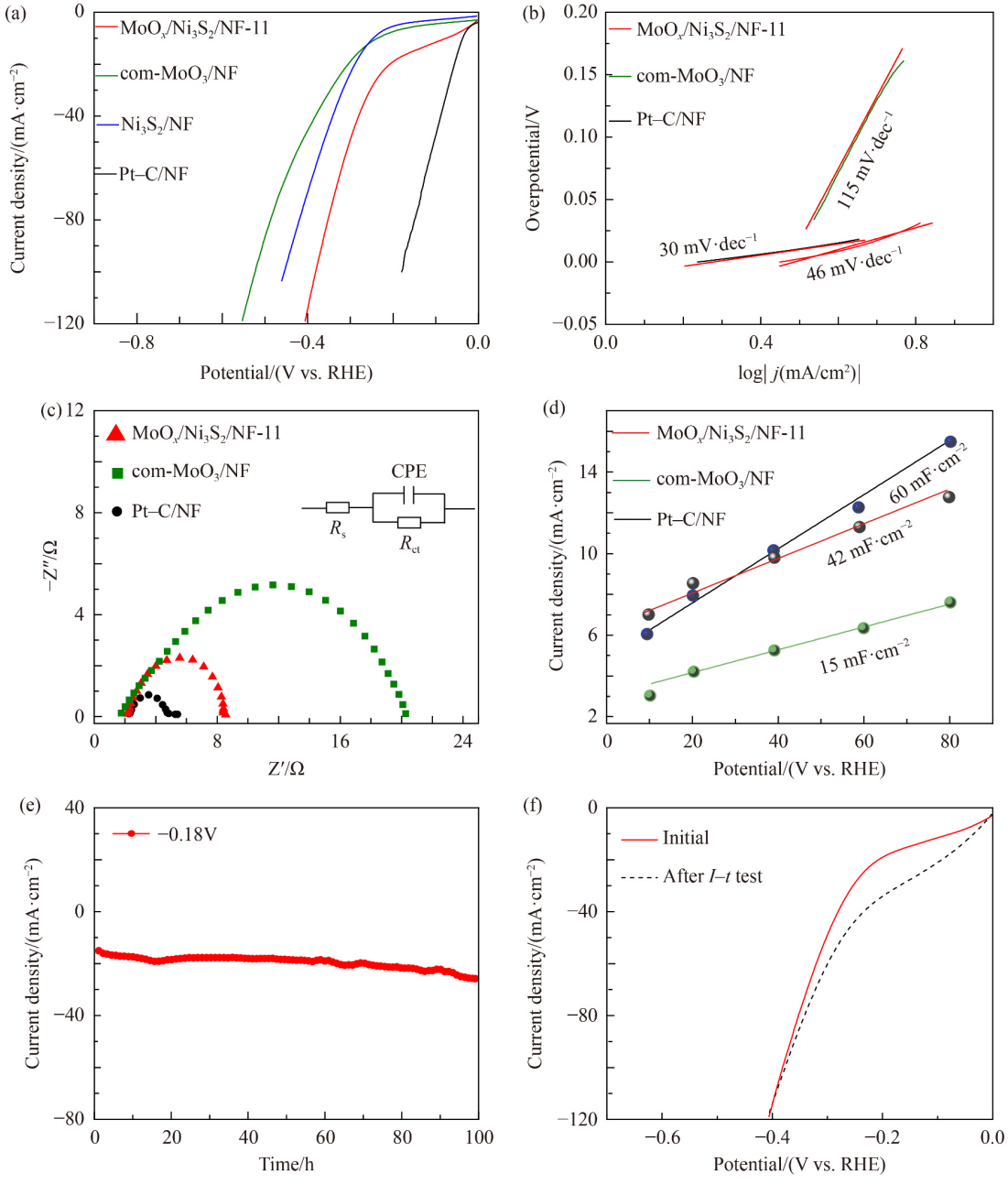

Fig. 5 (a) Polarization curves of MoO_x/Ni_3S_2/NF-11, com-MoO_3/NF, Ni_3S_2/NF and Pt–C/NF; (b) Tafel slopes of MoO_x/Ni_3S_2/NF-11, com-MoO_3/NF and Pt–C/NF derived from polarization curves; (c) Nyquist plots of MoO_x/Ni_3S_2/NF-11, com-MoO_3/NF and Pt–C/NF at –200 mV versus RHE measured from electrochemical impedance spectroscopy (EIS) in the frequency range from 10^5 to 0.01 Hz; (d) plots of current density as a function of scan rates for MoO_x/Ni_3S_2/NF-11, com-MoO_3/NF and Pt–C/NF; (e) chronoamperometric curve of MoO_x/Ni_3S_2/NF-11 at a constant applied potential of –180 mV versus RHE; (f) polarization curves of before and after 100 h *I–t* test of MoO_x/Ni_3S_2/NF-11. All the measurements were performed in a 0.5 mol·L^{-1} H_2SO_4 electrolyte.

MoO_x/Ni_3S_2/NF-01 (η_{10} = 127 mV) without ethanol added during synthesis and MoO_x/Ni_3S_2/NF-21 (η_{10} = 114 mV) prepared at an ethanol:H_2O ratio of 2:1. From the SEM images mentioned above, the MoO_x/Ni_3S_2/NF-11 has a relatively small particle size and no crack on the surface, which is conducive to increasing the contact area between the catalyst and the electrolyte and accelerating the electron transmission. Therefore, the MoO_x/Ni_3S_2/NF-11 exhibits the optimal HER performance. Furthermore, the η_{10} of 76 mV of MoO_x/Ni_3S_2/NF-11 is extremely lower than that (235 mV) of com-MoO_3/NF, and is close to that (37 mV) of Pt–C/NF, showing performance exceeding com-MoO_3 and comparable to Pt–C. As listed in Table 1 [16,17,41–46], the η_{10} of MoO_x/Ni_3S_2/NF-11 is obviously lower compared with the reported Mo-related electrocatalysts. The excellent catalytic performance of MoO_x/Ni_3S_2/NF-11 may be mainly attributed to the oxygen vacancy. For the P-MoO_3 [16], though it also contains oxygen vacancies coming from P doping, it has a larger η_{10} of 166 mV, meaning an inferior HER activity than MoO_x/Ni_3S_2/NF-11. The outstanding HER activity of MoO_x/Ni_3S_2/NF-11 suggests that there may be heterojunctions formed in the two integrated phases of MoO_3 and Ni_3S_2. The heterojunction and oxygen vacancy would offer rapid electron transfer favorable to the HER activity.

To explore the catalytic mechanism of the electrocatalysts, Tafel plots were calculated (Fig. 5(b)). The Tafel slope of MoO_x/Ni_3S_2/NF-11 is 46 mV·dec^{-1}, which is close to the value (30 mV·dec^{-1}) of Pt–C/NF and much lower than that (115 mV·dec^{-1}) of com-MoO_3/NF. Table 1 listed the Tafel slopes of reported Mo-based HER catalysts. The low Tafel slope of MoO_x/Ni_3S_2/NF-11 demonstrates its effectively enhanced kinetics during the H_2O dissociation [17]. On the basis of kinetic models, the Tafel slopes of 120, 40 and 30 mV·dec^{-1} are assigned to Volmer (Eq. (3)), Heyrovsky (Eq. (4)) and Tafel (Eq. (5)) reactions, respectively:

$$H_3O^+ + * + e^- \rightarrow H_{ads}* + H_2O \quad (3)$$

$$H_{ads}* + H_3O^+ + e^- \rightarrow * + H_2 + H_2O \quad (4)$$

$$H_{ads}* + H_{ads}* \rightarrow 2* + H_2\uparrow \quad (5)$$

The first step is Volmer reaction (Eq. (3)), for which one proton (H_3O^+) first adsorbs on the surface of the catalyst and accepts one electron to generate one hydrogen atom (H_{ads}*). The second step involves two kinds of reactions: one is Heyrovsky reaction and the other is Tafel reaction. For the Heyrovsky reaction (Eq. (4)), which is an electrochemical desorption, another proton (H_3O^+) accepts one electron and desorbs from catalyst surface and react with the former H atom to generate one H_2. For the Tafel step (Eq. (5)), two H_{ads} desorb from catalyst surface and combine directly and then release one H_2. The slope of 46 mV·dec^{-1} for MoO_x/Ni_3S_2/NF-11 indicates it follows the Volmer–Heyrovsky mechanism, while Pt–C/NF with the much lower slope of 30 mV·dec^{-1} follows the Volmer–Tafel mechanism. Nyquist plots were obtained by measuring EIS and the charge-transfer resistance (R_{ct}) values were fitted by the equivalent circuit model (Fig. 5(c)). It can be seen that the MoO_x/Ni_3S_2/NF-11 shows an extremely small R_{ct} of 6.51 Ω, which is much lower than the com-MoO_3/NF (21.51 Ω), indicating that the MoO_x/Ni_3S_2/NF-11 has faster charge transfer dynamics in HER process (see Table S2, cf. ESM). The fast charge transfer is probably attributed to synergetic effect of the amorphous MoO_x and the Ni_3S_2 nanoparticles. The abundant interfaces of the two phases make the hydrogen adsorption and desorption more effective [17].

In general, good electrocatalytic activity is accompanied by a large electrochemically active surface area, which is normally proportional to the electrochemical double-layer capacitance (C_{dl}). From the cyclic voltammetry curves carried out at varied scan rates (Fig. S7, cf. ESM), the C_{dl} of MoO_x/Ni_3S_2/NF-11 is calculated as 42 mF·cm^{-2} (Fig. 5(d)). This C_{dl} value is much larger than those many reported catalysts, such as MoO_3 (13.58 mF·cm^{-2}) [14], UDSL-MoS_2-rGO (24 mF·cm^{-2}) [42], MoP/NG (9.1 mF·cm^{-2}) [45] and $MoO_2/MoSe_2$ (18.68 μF·cm^{-2}) [47]. This large C_{dl} unveils the large amount of electrochemical active sites in the MoO_x/Ni_3S_2/NF-11. These results reveal that the MoO_x/Ni_3S_2/NF-11 with oxygen vacancies generates more accessible active sites, thereby promoting the H_2 evolution process.

Table 1 HER performance of MoO_x/Ni_3S_2/NF-11 and some reported electrocatalysts in 0.5 mol·L^{-1} H_2SO_4

Catalysts	η_{10}/mV	Tafel slope/(mV·dec^{-1})	Ref.
MoO_x/Ni_3S_2/NF-11	76	46	This work
P-MoO_{3-x} a)	166	42	[11]
MoO_3@RuO_2 b)	110	62	[17]
Pd NDs/DR MoS_2 c)	103	41	[41]
UDSL-MoS_2-rGO d)	ca. 210	35	[42]
Mo/Mo_2C e)	89	62	[43]
(1T/2H) MoS_2/α-MoO_3 f)	232	81	[44]
MoP/NG g)	94	50	[45]
MoC_x h)	142	53	[46]

a) P doped MoO_{3-x}, prepared via two-step intercalation method by using dodecylamine (DDA) and 4-bromine benzyl phosphoric acid; b) RuO_2 nanoparticles supported on MoO_3 nanosheets, prepared by a sonochemical method followed by calcination in air; c) Pd nanodisks (NDs) assembled on the basal plane of defect-rich MoS_2 nanosheets (DR-MoS_2); d) ultradispersed and single-layered MoS_2 nanoflakes coupled with reduced graphene oxide sheets (UDSL-MoS_2-rGO), synthesized by a hydrothermal method using $(NH_4)_6Mo_7O_{24}\cdot 4H_2O$, L-cysteine and GO under pH = 1; e) Mo/Mo_2C heteronanosheets, obtained by a NaCl template method followed by the reduction and carbonization under H_2 and CH_4, respectively; f) (1T/2H) MoS_2/α-MoO_3 prepared by hydrothermal method using thiourea, MoO_3 and $N_2H_4\cdot H_2O$; g) MoP nanoflakes intercalated nitrogen-doped graphene nanobelts (MoP/NG), synthesized by inserting DDA into MoO_3 nanobelts followed by phosphorization; h) MoC_x obtained by MOFs-assisted strategy followed by annealing under N_2 flow.

3.3 DFT calculations

DFT calculations (Fig. 6) were employed to well understand the influence of oxygen vacancy and Ni_3S_2 component on the catalytic activity. According to TEM characterization, MoO_x was found to be wrapped outside the Ni_3S_2. Therefore, when building the optimized models, the possibility of H^* adsorption on MoO_3 is given priority, and Ni_3S_2 is regarded as the "substrate" of MoO_3. As shown in Figs. 6(A), we calculate the ΔG_{H^*} of MoO_3 (on O site), oxygen-deficient MoO_3 (noted as O_v-MoO_3, on Mo site), MoO_3/Ni_3S_2 (on O site), and O_v-MoO_3/Ni_3S_2 (on O and Mo sites). The MoO_3 (Fig. 6(A-a)) shows a ΔG_{H^*} of –2.37 eV, for which the negative value indicates easy H adsorption (Volmer reaction, Eq. (3) discussed above) but difficult H desorption (Heyrovsky reaction, Eq. (4) discussed above). Because the surface of MoO_3 is all O atoms and the O–H^* bond is strong, the H^* is difficult to be desorbed. At this time, desorption step becomes the rate-determining step. When oxygen vacancy is present, as in O_v-MoO_3 (Fig. 6(A-b)), Mo sites are exposed to exhibit a smaller $|\Delta G_{H^*}|$ of 2.30 eV. When MoO_3 and Ni_3S_2 form the heterojunction (Fig. 6(A-c), the MoO_3/Ni_3S_2 has a much smaller $|\Delta G_{H^*}|$ of 1.82 eV, which means weakened binding between O and H, thus facilitating the H desorption. While for the heterojunction of O_v-MoO_3/Ni_3S_2 containing oxygen vacancy, $|\Delta G_{H^*}|$ on the O site adjacent to oxygen vacancy is slightly increased to 1.98 eV (Fig. 6(A-d)), indicating strengthened O–H bonding (difficult H desorption). More importantly and interestingly, the Mo site of O_v-MoO_3/Ni_3S_2 has a much lower $|\Delta G_{H^*}|$ of 1.54 eV (Fig. 6(A-e)), which is the most close to the value of 0. As known an electrocatalyst with $|\Delta G_{H^*}|$ approaching to zero would have high HER activity. So the exposed Mo due to oxygen defect serves as active sites. By comparing (a) and (c), or (b) and (d) in Fig. 6(A), it can be seen that the heterojunction greatly improves the catalytic activity of both O and Mo sites, while comparison of (c), (d) and (e) in Fig. 6(A) shows that although oxygen deficiency slightly reduces the activity of O sites, the exposed Mo sites result in much better catalytic activity.

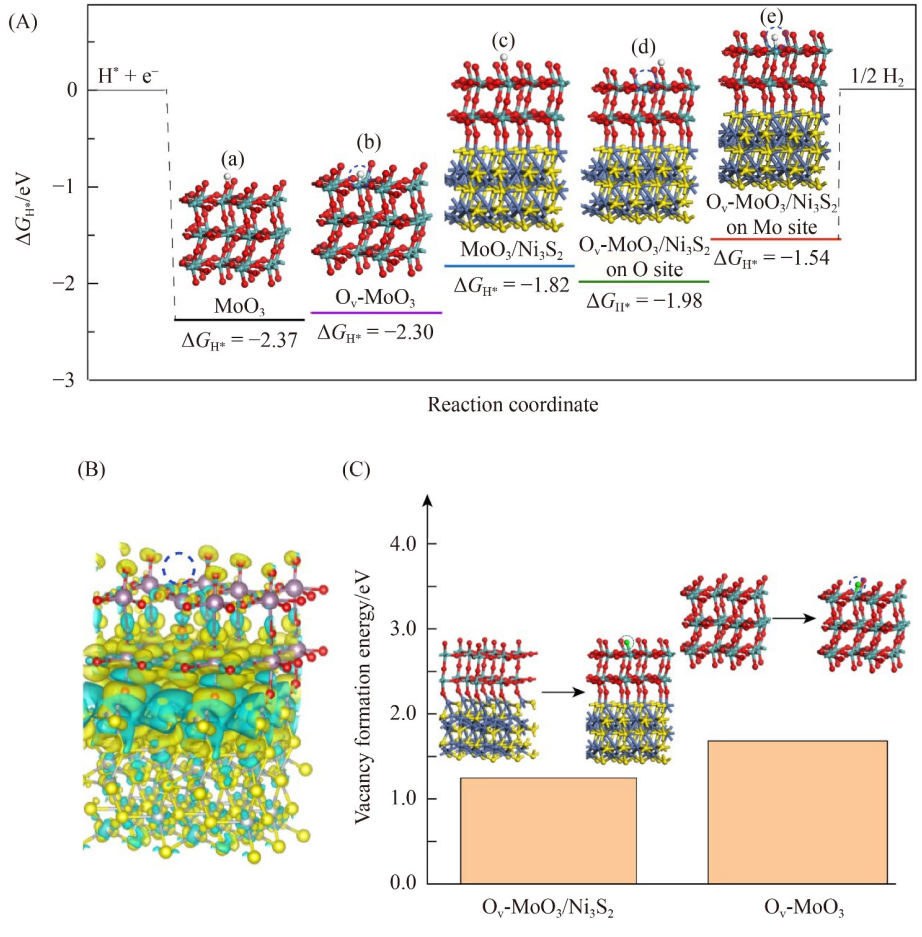

Fig. 6 (A) Optimized structures of (a) MoO_3, (b) O_v-MoO_3, (c) MoO_3/Ni_3S_2, (d) O_v-MoO_3/Ni_3S_2 with H^* on O site and (e) O_v-MoO_3/Ni_3S_2 with H^* on Mo site and the corresponding H adsorption free energy (ΔG_{H^*}) at a potential $U = 0$ V relative to standard hydrogen electrode at pH = 0; (B) differential charge density distribution of O_v-MoO_3/Ni_3S_2; (C) vacancy formation energy of O_v-MoO_3/Ni_3S_2 and O_v-MoO_3 and corresponding models. Symbols for atoms: Mo is cyan in A and C while purple in B, S is yellow, Ni is blue in A and C while grey in B, O is red and H^* is white. The dotted box shows the position of oxygen vacancy.

Differential charge density distribution of the O_v-MoO_3/Ni_3S_2 has been calculated, with results shown in Fig. 6(B). It is found that there is a strong charge transfer between Ni_3S_2 and MoO_3. Compared with MoO_3/Ni_3S_2 (without oxygen vacancy, Fig. S8, cf. ESM), the O atoms in O_v-MoO_3/Ni_3S_2 (Fig. 6(B)) gain more electrons. The increase of surface charge of oxygen will strengthen the binding of O–H and make the desorption more difficult. This is the reason why the $|\Delta G_{H^*}|$ on O site of O_v-MoO_3/Ni_3S_2 is larger than that of MoO_3/Ni_3S_2. In addition, Fig. 6(B) depicts electron deficiency of exposed Mo site in O_v-MoO_3/Ni_3S_2. During the Heyrovsky reaction, Mo–H^* bond needs to be dissociated prior to H_2 release. In this process, electrophilic Mo will pull the electrons between Mo and H, which will weaken the Mo–H^* bond thus promoting hydrogen evolution via the cleavage of Mo–H^* [48].

Long-term durability is another crucial requirement for the catalysts in real applications. To measure the durability of MoO_x/Ni_3S_2/NF-11, the time-dependent current density was measured at a constant potential of –0.18 V for 100 h. The excellent stability is due to that the acid-resistant amorphous MoO_x encases the Ni_3S_2 and NF substrate which are unstable under acidic conditions. As seen in Fig. 5(e), the MoO_x/Ni_3S_2/NF-11 was continuously operated for 100 h with no significant degradation observed, confirming the ultra-durable stability. Figure 5(f) shows the linear sweep voltammetry before and after 100 h *I–t* HER test. As observed, the catalytic activity of the MoO_x/Ni_3S_2/NF-11 was even increased after the stability test. This may be thankful to the surface reconfiguration of the catalyst [49]. In order to deeply learn about the reaction mechanism in the HER process, we have carried out SEM and XPS for MoO_x/Ni_3S_2/NF-11 after stability test. From the SEM images shown in Fig. S9 (cf. ESM), we see after the HER test, the microstructure of MoO_x/Ni_3S_2/NF-11 has not changed significantly, and many irregular small spheres are still attached to the surface of NF. From XPS (Fig. 7), after long-term stability test (100 h), the valence states of Ni and S do not change [50]. For Mo, the mixed valence state of Mo^{5+} and Mo^{6+} is still reflected after the stability test. The peaks at 235.6 and 232.4 eV correspond to Mo^{6+} [28], and the binding energies of 234.0 and 230.8 eV are related to Mo^{5+} [29]. At the same time, it can be seen from the integral area of the curve that the content of Mo^{5+} increases compared with that before. In addition, the O 1s peaks shift towards lower binding energy by 0.2 eV after stability test. The increase of Mo^{5+} content and the shift of O 1s with lower binding energy also prove that the oxygen vacancy content increased after long-term stability. The *in situ* surface reconfiguration may result in more oxygen vacancies on catalyst surface, which exposes more Mo active sites. EPR spectroscopy (Fig. 3(h)) shows that the MoO_x/Ni_3S_2/NF-11 after 60 h *I–t* test displays a much stronger signal, proving increased content of oxygen vacancy in the catalyst after HER testing, which is consistent with the XPS characterization. To further confirm the *in situ* surface reconfiguration of the catalyst, we calculated the formation energy of oxygen vacancy in MoO_3 and MoO_3/Ni_3S_2. As shown in Fig. 6(C), when MoO_3 and Ni_3S_2 form heterojunction, the formation energy of oxygen vacancy is significantly reduced, and thus decreases the energy barrier for structural reconfiguration. This will enable MoO_3 to have more oxygen vacancies, thus exposing more active sites of Mo. The low $|\Delta G_{H^*}|$ of exposed Mo sites is beneficial to the improvement of the HER activity. With the continuation of the electrolysis reactions, the performance of the catalyst will gradually improve. From the long-term durability test (Fig. 5(e)), the initial current density is 18.2 $mA \cdot cm^{-2}$, while until 100 h, the current density increases to 23.5 $mA \cdot cm^{-2}$. This phenomenon confirms the rationality of the above conjecture. The higher durability of the MoO_x/Ni_3S_2/NF-11 than that of the existing catalysts endows it a broad application.

Overall, from the above results we see clearly that the electrocatalytic performance of the MoO_x/Ni_3S_2/NF-11 material exceeds most known transition metal sulfides and oxides catalysts. Benefiting from the oxygen vacancy and heterostructure, the exposed Mo sites exhibit much reduced $|\Delta G_{H^*}|$, which endows the function as active sites, leading to the excellent HER performance. The outstanding catalytic activity and wonderful durability of MoO_x/Ni_3S_2/NF-11 demonstrate it is a promising electrocatalyst for HER.

4 Conclusions

In summary, by a facile and cost-effective solvothermal method, amorphous and oxygen-deficient MoO_x integrated with Ni_3S_2 nanoparticles are embedded in the Ni foam to fabricate the new electrocatalysts of MoO_x/Ni_3S_2/NF-*mn*. The optimum oxygen-deficient MoO_x/Ni_3S_2/NF-11 exhibits remarkable HER activity, requiring a much low η_{10} value of 76 mV and an extremely small Tafel slope of 46 $mV \cdot dec^{-1}$ in acidic media. The oxygen vacancy leaves the Mo sites exposed, and the reduced $|\Delta G_{H^*}|$ of Mo sites ensures the enhancement of HER activity. Moreover, the formed MoO_x/Ni_3S_2 heterostructure further reduces the $|\Delta G_{H^*}|$ of Mo and O sites, which is another key factor in improving the catalytic activity. The high activity of MoO_x/Ni_3S_2/NF-11 can be maintained for more than 100 h at constant potential of 180 mV. The outside acid-resistant MoO_x layer encases the inside Ni_3S_2 and NF which are unstable under acidic conditions, thus increasing the acid resistance of the overall catalyst. In addition, the heterostructure can effectively reduce the formation energy of oxygen vacancy, which leads to the *in situ* reconstruction of the catalysts during the electrocatalytic process, thus

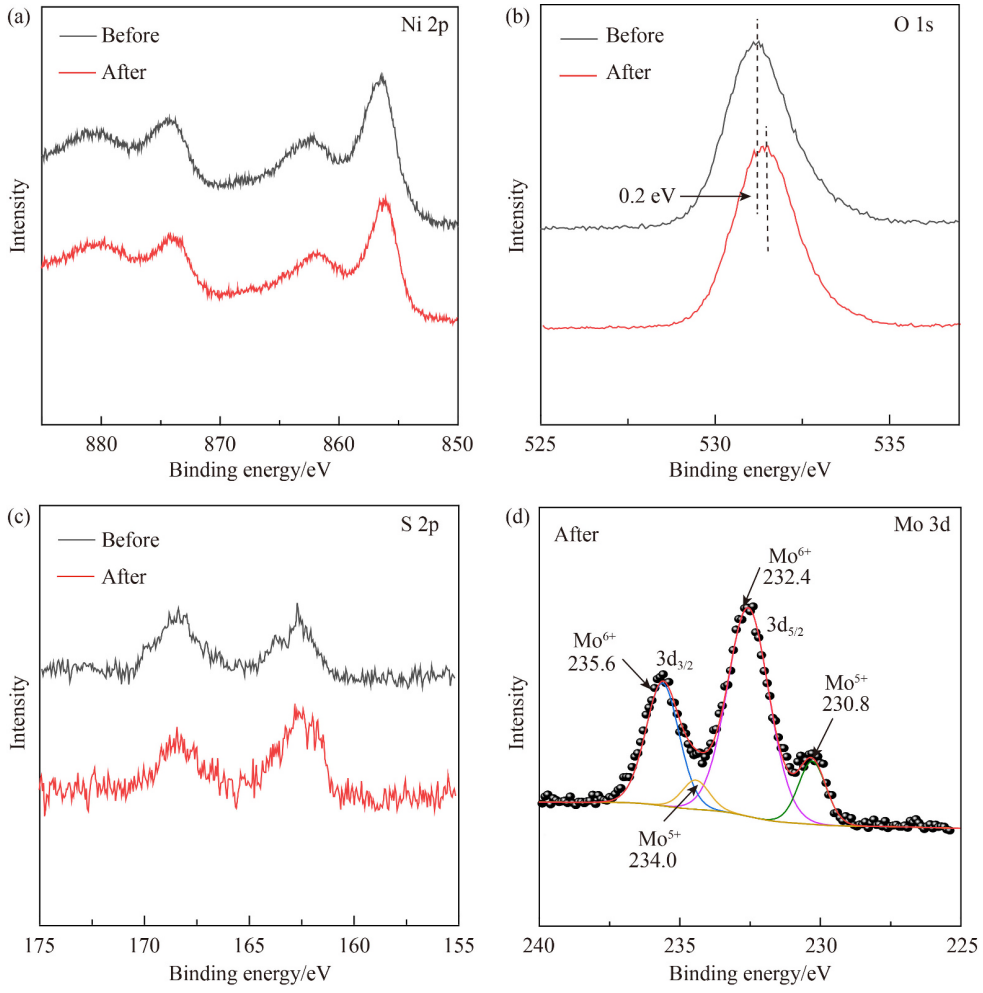

Fig. 7 XPS spectra of (a) Ni 2p, (b) O 1s, and (c) S 2p for MoO_x/Ni_3S_2/NF-11 before and after HER testing, and (d) Mo 3d for MoO_x/Ni_3S_2/NF-11 after HER testing.

promoting HER performance. As a high-performance and ultra-durable electrocatalyst, MoO_x/Ni_3S_2/NF-11 might be regarded as a cost-effective candidate to take the place of noble metals catalysts used in HER. This work could provide new ideas for the design of other oxygen-deficient materials, therefore starting new opportunities to develop high-performance materials for HER or other applications.

Acknowledgements Experimental work is supported by the National Natural Science Foundation of China (Grant No. 22176017), Scientific Research Project of the Ningxia Higher Education Department of China (Grant No. NGY2020034) and CAS "Light of West China Program (Grant No. XAB2020YW16)".

Electronic Supplementary Material Supplementary material is available in the online version of this article at https://dx.doi.org/10.1007/s11705-022-2228-1 and is accessible for authorized users.

References

1. Zou X, Zhang Y. Noble metal-free hydrogen evolution catalysts for water splitting. Chemical Society Reviews, 2015, 44(15): 5148–5180
2. Turner J A. Sustainable hydrogen production. Science, 2004, 305(5686): 972–974
3. Holladay J D, Hu J, King D L, Wang Y. An overview of hydrogen production technologies. Catalysis Today, 2009, 139(4): 244–260
4. Chen W F, Muckerman J T, Fujita E. Recent developments in transition metal carbides and nitrides as hydrogen evolution electrocatalysts. Chemical Communications, 2013, 49(79): 8896–8909
5. Zhang J, Wang T, Liu P, Liao Z, Liu S, Zhuang X, Chen M, Zschech E, Feng X. Efficient hydrogen production on $MoNi_4$ electrocatalysts with fast water dissociation kinetics. Nature Communications, 2017, 8(1): 15437
6. Stamenkovic V R, Mun B S, Arenz M, Mayrhofer K J J, Lucas C A, Wang G F, Ross P N, Markovic N M. Trends in electrocatalysis on extended and nanoscale Pt-bimetallic alloy surfaces. Nature Materials, 2007, 6(3): 241–247
7. Wang K W, She X L, Chen S, Liu H L, Li D H, Wang Y, Zhang H W, Yang D J, Yao X D. Boosting hydrogen evolution via optimized hydrogen adsorption at the interface of CoP_3 and Ni_2P.

Journal of Materials Chemistry A: Materials for Energy and Sustainability, 2018, 6(14): 5560–5565

8. Lu W, Song Y, Dou M, Ji J, Wang F. Ni_3S_2@MoO_3 core/shell arrays on Ni foam modified with ultrathin CdS layer as a superior electrocatalyst for hydrogen evolution reaction. Chemical Communications, 2018, 54(6): 646–649
9. Wang X, Ma W, Ding C, Xu Z, Wang H, Zong X, Li C. Amorphous multi-elements electrocatalysts with tunable bifunctionality toward overall water splitting. ACS Catalysis, 2018, 8(11): 9926–9935
10. Liang Q, Jin H, Wang Z, Xiong Y, Yuan S, Zeng X, He D, Mu S. Metal–organic frameworks derived reverse-encapsulation Co-NC@Mo_2C complex for efficient overall water splitting. Nano Energy, 2019, 57: 746–752
11. Li L, Zhang T, Yan J, Cai X, Liu S. P doped MoO_{3-x} nanosheets as efficient and stable electrocatalysts for hydrogen evolution. Small, 2017, 13(25): 1700441
12. Sinaim H, Ham D J, Lee J S, Phuruangrat A, Thongtem S, Thongtem T. Free-polymer controlling morphology of α-MoO_3 nanobelts by a facile hydrothermal synthesis, their electrochemistry for hydrogen evolution reactions and optical properties. Journal of Alloys and Compounds, 2012, 516: 172–178
13. Zhu Y H, Yao Y, Luo Z, Pan C Q, Yang J, Fang Y R, Deng H T, Liu C X, Tan Q, Liu F D, Guo Y. Nanostructured MoO_3 for efficient energy and environmental catalysis. Molecules, 2020, 25(1): 26
14. Li J, Cheng Y, Zhang J, Fu J, Yan W, Xu Q. Confining Pd nanoparticles and atomically dispersed Pd into defective MoO_3 nanosheet for enhancing electro- and photocatalytic hydrogen evolution performances. ACS Applied Materials & Interfaces, 2019, 11(31): 27798–27804
15. Xue X, Zhang J, Saana I A, Sun J, Xu Q, Mu S. Rational inert-basal-plane activating design of ultrathin 1T′ phase MoS_2 with a MoO_3 heterostructure for enhancing hydrogen evolution performances. Nanoscale, 2018, 10(35): 16531–16538
16. Liu P T, Zhu J Y, Zhang J Y, Xi P X, Tao K, Gao D Q, Xue D S. P dopants triggered new basal plane active sites and enlarged interlayer spacing in MoS_2 nanosheets toward electrocatalytic hydrogen evolution. ACS Energy Letters, 2017, 2(4): 745–752
17. Sadhanala H K, Harika V K, Penki T R, Aurbach D, Gedanken A. Ultrafine ruthenium oxide nanoparticles supported on molybdenum oxide nanosheets as highly efficient electrocatalyst for hydrogen evolution in acidic medium. ChemCatChem, 2019, 11(5): 1495–1502
18. Lim K J H, Yilmaz G, Lim Y F, Ho G W. Multi-compositional hierarchical nanostructured Ni_3S_2@MoS_x/NiO electrodes for enhanced electrocatalytic hydrogen generation and energy storage. Journal of Materials Chemistry A: Materials for Energy and Sustainability, 2018, 6(41): 20491–20499
19. Kou T, Smart T, Yao B, Chen I, Thota D, Ping Y, Li Y. Theoretical and experimental insight into the effect of nitrogen doping on hydrogen evolution activity of Ni_3S_2 in alkaline medium. Advanced Energy Materials, 2018, 8(19): 1703538
20. Feng L L, Yu G, Wu Y, Li G D, Li H, Sun Y, Asefa T, Chen W, Zou X. High-index faceted Ni_3S_2 nanosheet arrays as highly active and ultrastable electrocatalysts for water splitting. Journal of the American Chemical Society, 2015, 137(44): 14023–14026
21. Chang Y H, Lin C T, Chen T Y, Hsu C L, Lee Y H, Zhang W, Wei K H, Li L J. Highly efficient electrocatalytic hydrogen production by MoS_x grown on graphene-protected 3D Ni foams. Advanced Materials, 2013, 25(5): 756–760
22. Tang C, Pu Z, Liu Q, Asiri A M, Luo Y, Sun X. Ni_3S_2 nanosheets array supported on Ni foam: a novel efficient three-dimensional hydrogen-evolving electrocatalyst in both neutral and basic solutions. International Journal of Hydrogen Energy, 2015, 40(14): 4727–4732
23. Cao J, Zhou J, Zhang Y, Wang Y, Liu X. Dominating role of aligned MoS_2/Ni_3S_2 nanoarrays supported on three-dimensional Ni foam with hydrophilic interface for highly enhanced hydrogen evolution reaction. ACS Applied Materials & Interfaces, 2018, 10(2): 1752–1760
24. Yang Y, Yao H, Yu Z, Islam S M, He H, Yuan M, Yue Y, Xu K, Hao W, Sun G, Li H, Ma S, Zapol P, Kanatzidis M G. Hierarchical nanoassembly of $MoS_2/Co_9S_8/Ni_3S_2$/Ni as a highly efficient electrocatalyst for overall water splitting in a wide pH range. Journal of the American Chemical Society, 2019, 141(26): 10417–10430
25. Li T T, Zuo Y P, Lei X M, Li N, Liu J W, Han H Y. Regulating the oxidation degree of nickel foam: a smart strategy to controllably synthesize active Ni_3S_2 nanorod/nanowire arrays for high-performance supercapacitors. Journal of Materials Chemistry A: Materials for Energy and Sustainability, 2016, 4(21): 8029–8040
26. Tang T, Jiang W J, Niu S, Liu N, Luo H, Chen Y Y, Jin S F, Gao F, Wan L J, Hu J S. Electronic and morphological dual modulation of cobalt carbonate hydroxides by Mn doping toward highly efficient and stable bifunctional electrocatalysts for overall water splitting. Journal of the American Chemical Society, 2017, 139(24): 8320–8328
27. He W, Wang C, Li H, Deng X, Xu X, Zhai T. Ultrathin and porous $Ni_3S_2/CoNi_2S_4$ 3D-network structure for superhigh energy density asymmetric supercapacitors. Advanced Energy Materials, 2017, 7(21): 1700983
28. Yang J, Zhang F J, Wang X, He D S, Wu G, Yang Q H, Hong X, Wu Y, Li Y D. Porous molybdenum phosphide nano-octahedrons derived from confined phosphorization in UIO-66 for efficient hydrogen evolution. Angewandte Chemie International Edition, 2016, 55(41): 12854–12858
29. Weber T, Muijsers J C, Niemantsverdriet J W. Structure of amorphous MoS_3. Journal of Physical Chemistry, 1995, 99(22): 9194–9200
30. Li L D, Yan J Q, Wang T, Zhao Z J, Zhang J, Gong J L, Guan N J. Sub-10 nm rutile titanium dioxide nanoparticles for efficient visible-light-driven photocatalytic hydrogen production. Nature Communications, 2015, 6(1): 10
31. Li J, Cheng Y, Zhang J, Fu J, Yan W, Xu Q. Confining Pd Nanoparticles and atomically dispersed Pd into defective MoO_3 nanosheet for enhancing electro- and photocatalytic hydrogen evolution performances. ACS Applied Materials & Interfaces, 2019, 11(31): 27798–27804
32. Kang Q, Cao J Y, Zhang Y J, Liu L Q, Xu H, Ye J H. Reduced

TiO_2 nanotube arrays for photoelectrochemical water splitting. Journal of Materials Chemistry A: Materials for Energy and Sustainability, 2013, 1(18): 5766–5774

33. Yan J Q, Zhang Y X, Liu S Z, Wu G J, Li L D, Guan N J. Facile synthesis of an iron doped rutile TiO_2 photocatalyst for enhanced visible-light-driven water oxidation. Journal of Materials Chemistry A: Materials for Energy and Sustainability, 2015, 3(43): 21434–21438
34. Xie F, Wu H, Mou J, Lin D, Xu C, Wu C, Sun X. Ni_3N@Ni-Ci nanoarray as a highly active and durable non-noble-metal electrocatalyst for water oxidation at near-neutral pH. Journal of Catalysis, 2017, 356: 165–172
35. Zhou W, Wu X J, Cao X, Huang X, Tan C, Tian J, Liu H, Wang J, Zhang H. Ni_3S_2 nanorods/Ni foam composite electrode with low overpotential for electrocatalytic oxygen evolution. Energy & Environmental Science, 2013, 6(10): 2921
36. Chia X, Sutrisnoh N A A, Pumera M. Tunable Pt-MoS_x hybrid catalysts for hydrogen evolution. ACS Applied Materials & Interfaces, 2018, 10(10): 8702–8711
37. Kuang P Y, Tong T, Fan K, Yu J G. *In situ* fabrication of Ni−Mo bimetal sulfide hybrid as an efficient electrocatalyst for hydrogen evolution over a wide pH range. ACS Catalysis, 2017, 7(9): 6179–6187
38. Wang B, Huang H, Sun T, Yan P, Isimjan T T, Tian J, Yang X. Dissolution reconstruction of electron-transfer enhanced hierarchical NiS_x−MoO_2 nanosponges as a promising industrialized hydrogen evolution catalyst beyond Pt/C. Journal of Colloid and Interface Science, 2020, 567: 339–346
39. Cheng Z, Abernathy H, Liu M L. Raman spectroscopy of nickel sulfide Ni_3S_2. Journal of Physical Chemistry C, 2007, 111(49): 17997–18000
40. Li Z, Ma J, Zhang B, Song C, Wang D. Crystal phase- and morphology-controlled synthesis of MoO_3 materials. CrystEngComm, 2017, 19(11): 1479–1485
41. Qi K, Yu S S, Wang Q Y, Zhang W, Fan J C, Zheng W T, Cui X Q. Decoration of the inert basal plane of defect-rich MoS_2 with Pd atoms for achieving Pt-similar HER activity. Journal of Materials Chemistry A: Materials for Energy and Sustainability, 2016, 4(11): 4025–4031
42. Huang H L, Huang J Y, Liu W P, Fang Y P, Liu Y. Ultradispersed and single-layered MoS_2 nanoflakes strongly coupled with graphene: an optimized structure with high kinetics for the hydrogen evolution reaction. ACS Applied Materials & Interfaces, 2017, 9(45): 39380–39390
43. Xiong J, Li J, Shi J W, Zhang X L, Suen N T, Liu Z, Huang Y J, Xu G X, Cai W W, Lei X R, Feng L, Yang Z, Huang L, Cheng H. *In situ* engineering of double-phase interface in Mo/Mo_2C heteronanosheets for boosted hydrogen evolution reaction. ACS Energy Letters, 2018, 3(2): 341–348
44. Manikandan A, Ilango P R, Chen C W, Wang Y C, Shih Y C, Lee L, Wang Z M M, Ko H, Chueh Y L. A superior dye adsorbent towards the hydrogen evolution reaction combining active sites and phase-engineering of (1T/2H) MoS_2/MoO_3 hybrid heterostructured nanoflowers. Journal of Materials Chemistry A: Materials for Energy and Sustainability, 2018, 6(31): 15320–15329
45. Huang C, Pi C R, Zhang X M, Ding K, Qin P, Fu J J, Peng X, Gao B, Chu P K, Huo K F. *In situ* synthesis of MoP nanoflakes intercalated N-doped graphene nanobelts from MoO_3-amine hybrid for high-efficient hydrogen evolution reaction. Small, 2018, 14(25): 7
46. Wu H B, Xia B Y, Yu L, Yu X Y, Lou X W. Porous molybdenum carbide nano-octahedrons synthesized via confined carburization in metal−organic frameworks for efficient hydrogen production. Nature Communications, 2015, 6(1): 8
47. Chen X, Liu G, Zheng W, Feng W, Cao W, Hu W, Hu P. Vertical 2D MoO_2/$MoSe_2$ core-shell nanosheet arrays as high-performance electrocatalysts for hydrogen evolution reaction. Advanced Functional Materials, 2016, 26(46): 8537–8544
48. Zhu L F, Liu L J, Huang G M, Zhao Q. Hydrogen evolution over N-doped CoS_2 nanosheets enhanced by superaerophobicity and electronic modulation. Applied Surface Science, 2020, 504: 144490
49. He L, Zhang W, Mo Q, Huang W, Yang L, Gao Q. Molybdenum carbide-oxide heterostructures: *in situ* surface reconfiguration toward efficient electrocatalytic hydrogen evolution. Angewandte Chemie International Edition, 2020, 59(9): 3544–3548
50. Yilmaz G, Yang T, Du Y, Yu X, Feng Y, Shen L, Ho G. Stimulated electrocatalytic hydrogen evolution activity of MOF-derived MoS_2 basal domains via charge injection through surface functionalization and heteroatom doping. Advancement of Science, 2019, 6(15): 1900140